

# Secret Key Rate Analysis of RIS-Assisted THz MIMO CV-QKD Systems under Localized and Global Eavesdropping

Sushil Kumar, Soumya P. Dash, *Senior Member, IEEE*, and George C. Alexandropoulos, *Senior Member, IEEE*

**Abstract**—A multiple-input multiple-output (MIMO) system operating at terahertz (THz) frequencies and consisting of a transmitter, Alice, that encodes secret keys using Gaussian-modulated coherent states, which are communicated to a legitimate receiver, Bob, under the assistance of a reconfigurable intelligent surface (RIS) is considered in this paper. The composite wireless channel comprising the direct Alice-to-Bob signal propagation path and the RIS-enabled reflected one is modeled as a passive linear Gaussian quantum channel, allowing for a unitary dilation that preserves the canonical commutation relations. The security of the considered RIS-empowered MIMO system is analyzed under collective Gaussian entangling attacks, according to which an eavesdropper, Eve, is assumed to have access to environmental modes associated with specific propagation segments. We also study, as a benchmark, the case where Eve has access to the purification of the overall channel. The legitimate receiver, Bob, is designed to deploy homodyne detection and reverse reconciliation for key extraction. Novel expressions for the achievable secret key rate (SKR) of the system are derived for both the considered eavesdropping scenarios. Furthermore, an optimization framework is developed to determine the optimal RIS phase configuration matrix that maximizes the SKR performance. The resulting optimization problem is efficiently solved using particle swarm optimization. Numerical results are presented to demonstrate the system's performance with respect to various free parameters. It is showcased that the considered RIS plays a crucial role in enhancing the SKR of the system as well as in extending the secure communication range. This establishes RIS-assisted THz MIMO CV-QKD as a promising solution for next generation secure wireless networks.

**Index Terms**—Continuous variable quantum key distribution, multiple-input multiple-output, quantum communications, reconfigurable intelligent surfaces, secret key rate.

## I. INTRODUCTION

The advent of novel technologies for beyond fifth-generation (5G) and sixth-generation (6G) wireless communication systems is driven by the need to achieve high data rates, ultra-low latency, and high energy and spectral efficiencies [2], [3]. This has led to an increased interest in developing various physical layer techniques, namely extremely multiple-input multiple-output (MIMO) [4], [5], operation at terahertz (THz) frequencies [6], [7], integrated sensing and communications (ISAC) [8], [9], non-coherent communications [10]–[13], and reconfigurable intelligent surfaces

(RIS) [14], [15]. Among them, RISs have shown immense potential to revolutionize wireless communications, leveraging vast arrays of response-tunable metamaterial elements that are electronically optimized in almost real time, manipulating electromagnetic waves propagation within the physical wireless channel [16], [17]. An RIS can strategically direct the beams toward designated users, thereby ensuring reliable communication with increased data rates, improved signal quality, extended coverage, and minimized interference [18]. Moreover, implementing RIS technology enables robust communication links for systems dominated by non-line-of-sight (NLoS) signal propagation [19]. This has led to the usage of RIS to improve the performance of MIMO, ISAC, and index modulation systems, as well as satellite networks [20]–[26].

Another crucial aspect and requirement for next generation communication systems is improving the security and privacy of transmitted data. Traditional higher-layer encryption techniques based on the Rivest-Shamir-Adleman (RSA) algorithm have been proven to be inefficient and easily decodable utilizing Shor's algorithm, owing to the rapid technological advancements in quantum computing [27], [28]. Moreover, the development of quantum computers has resulted in the usage of algorithms for physical layer encryption, such as Diffie and Hellman, to be inefficient due to their capacity to yield solutions to computationally hard discrete logarithmic problems in a short time [29]. To overcome these challenges and enhance data privacy, quantum key distribution (QKD), a technique leveraging the underlying principles of quantum superposition and entanglement, has been proposed in the literature to offer versatile secure communication [30]–[32].

QKD ensures the secure transmission of secret keys between two authenticated users, namely Alice and Bob, even in the presence of a potential eavesdropper, Eve. The literature on QKD classifies the available techniques into two categories, i.e., discrete variable QKD (DV-QKD) and continuous variable QKD (CV-QKD) [30], [33]. The DV-QKD approach relies on sources and detectors specifically designed for single photons, and encrypts confidential key information by utilizing the polarization or phase of a single photon. The secure key produced by the DV-QKD approach is guaranteed by the no-cloning theorem of quantum physics, preventing the possibility of making perfect replicas of non-orthogonal quantum states without introducing detectable noise [34], [35]. In contrast, a secret key is encoded using the quadratures of continuous variable Gaussian quantum states with the CV-QKD technique, and its security is ensured by Heisenberg's uncertainty principle [27], [36]. Owing to higher hardware compatibility with classical communication systems and the ability to offer superior key rates and overall performance in noisy environments, as well

A part of this work has been accepted for presentation at the upcoming IEEE WCNC 2026 [1].

S. Kumar and S. P. Dash are with the School of Electrical and Computer Sciences, Indian Institute of Technology Bhubaneswar, Argul, Khordha, 752050 India, (e-mails: {a24ec09010, spdash}@iitbbs.ac.in).

G. C. Alexandropoulos is with the Department of Informatics and Telecommunications, National and Kapodistrian University of Athens, Panepistimiopolis Ilissia, 16122 Athens, Greece and also with the Department of Electrical and Computer Engineering, University of Illinois Chicago, IL 60601, USA (e-mail: alexandg@di.uoa.gr).

as ease of implementation in higher frequency ranges, the CV-QKD approach becomes a natural choice for wireless systems over the DV-QKD one [37], [38].

Most QKD-enhanced wireless systems focus on applications that require point-to-point communications, such as satellite-to-earth, inter-satellite, inter-building, and free-space maritime channels [39]–[44], which are traditionally achieved via free-space optical (FSO) links [45]. However, it has been studied that THz communication is often preferred over FSO due to its better resilience to weather, NLoS capabilities, easier deployment (with less strict alignment), and ability to handle high data rates over short distances [46]. This has led to several studies for terrestrial and inter-satellite wireless systems appearing in the literature considering the usage of the THz band for secure communications using the CV-QKD technique [47]–[49]. However, these studies have reported achieving low secret key rates (SKRs) and short transmission distances for secret keys, due to several factors that degrade the channel within the considered frequency spectrum. These limitations have been shown to be overcome to some extent by the integration of MIMO with CV-QKD [50], [51]. MIMO FSO with DV-QKD has been studied in [52]. On another front, RISs have also been lately integrated with QKD. The authors in [53] introduced the idea of reduction of reflection loss with the use of RIS, and the authors in [54] studied channel estimation and RIS to aid QKD-based quantum communication in a THz MIMO system. However, there has been limited research on using RISs to improve the performance of CV-QKD systems operating in the THz frequency band [54].

Motivated by this research gap, in this paper, we explore a MIMO CV-QKD wireless communication system assisted by an RIS. In this system, the RIS facilitates the transmission of secret keys between the two parties, Alice and Bob, in addition to the direct communication channel they already have. We also take into account a possible eavesdropper, Eve, whose abilities are limited by their physical access to the propagation environment. Unlike Eve, which is assumed to have complete purification of the entire channel between Alice and Bob, we examine realistic scenarios of localized eavesdropping, in which Eve can only access a portion of the environmental modes associated with channel loss. Such constraints naturally arise in wireless systems due to geometric constraints, blockages, and deployment limitations, especially in RIS-assisted THz links [55].

This work extends our preliminary findings presented in [1], where we have examined a worst-case global eavesdropping model in which Eve targets the overall effective channel. This paper introduces a comprehensive framework encompassing both global and localized eavesdropping scenarios. Specifically, we model segment-wise channel loss through a global unitary dilation and analyze Eve’s information gain when they have access to only select environmental modes. The major contributions of this paper are summarized as follows:

- We propose an RIS-assisted THz MIMO CV-QKD framework in which Alice transmits a single quantum signal that propagates through a coherent superposition of the direct and RIS-assisted channel paths, which are modeled

as a global passive Gaussian channel that preserves canonical commutation relations.

- We develop an eavesdropping model based on unitary channel dilation, in which Eve can perform collective Gaussian entanglement attacks by accessing selected environmental modes associated with channel loss.
- We introduce and analyze localized eavesdropping scenarios, in which Eve is restricted to access a single propagation segment (Alice–Bob, Alice–RIS, or RIS–Bob), and derive closed-form expressions for the corresponding SKR under reverse reconciliation (RR) and homodyne detection.
- As a benchmark, we also consider a global eavesdropping scenario in which Eve holds full control over the purification of the effective end-to-end MIMO channel between Alice and Bob. To handle the complexity of the MIMO channel structure, we studied an SVD-based parallel channel. A detailed derivation and analysis of this framework have been established in our prior work [1].
- We derive analytical expressions for both the classical mutual information between Alice and Bob as well as the Holevo information between Bob and Eve, highlighting how Eve’s information gain depends on their physical access to environmental modes.
- An optimization framework based on a particle swarm optimization (PSO) algorithm for maximizing the achievable SKR performance in the RIS phase configuration is presented.

Our extensive numerical investigations corroborate the analysis presented in the paper, showcasing the effects of the RIS size on the SKR performance as well as the transmission distance between Alice and Bob.

The rest of the paper is organized as follows. The system model of the RIS-assisted MIMO CV-QKD system, the transmission of secret keys between Alice and Bob, and the considered eavesdropping models are detailed in Section II. The SKR analysis under both localized and global eavesdropping models, along with the PSO algorithm, is presented in Section III. Finally, Section IV includes our numerical results, followed by concluding remarks in Section V.

*Notation:* Boldface letters such as  $\mathbf{A} \in \mathbb{C}^{M \times N}$  and  $\mathbf{a} \in \mathbb{C}^{M \times 1}$  represent matrices and vectors, respectively. The  $\mathbf{A}^\dagger$  symbol stands for the conjugate transpose of  $\mathbf{A}$ , the  $\mathbf{A}^T$  symbol stands for the transpose, the  $\mathbf{A}^{-1*}$  symbol represents Moore–Penrose pseudo-inverse, and  $\mathbf{A} \otimes \mathbf{B}$  indicates the tensor product between  $\mathbf{A}$  and  $\mathbf{B}$ . The notations  $\mathbf{1}_{M \times N}$  and  $\mathbf{0}_{M \times N}$  represent a matrix consisting of all ones and all zeros, respectively, and  $j \triangleq \sqrt{-1}$  is the imaginary unit.  $\mathbf{I}_M$  represents a  $M \times M$  identity matrix, and  $\text{diag}(\mathbf{a})$  returns a  $M \times M$  diagonal matrix with the elements of  $\mathbf{a}$  on its principal diagonal.  $a^*$  represents the conjugate of  $a$ . Notation  $\langle X \cdot Y \rangle$  indicates the quantum correlation between  $X$  and  $Y$ , while  $\mathcal{N}(\boldsymbol{\mu}, \boldsymbol{\sigma}^2)$  represents the real multivariate Gaussian distribution, where  $\boldsymbol{\mu}$  is the mean vector and  $\boldsymbol{\sigma}^2$  is the covariance matrix.  $[\_, \_]$  is the canonical bosonic commutation,  $|\cdot|$  denotes the magnitude operator, and the operator  $\text{eig}(\cdot)$  computes the eigenvalues of a matrix. Furthermore,  $\hat{Q}$  denotes the operator (such as annihilation and creation) acting on the signal mode  $Q$ .

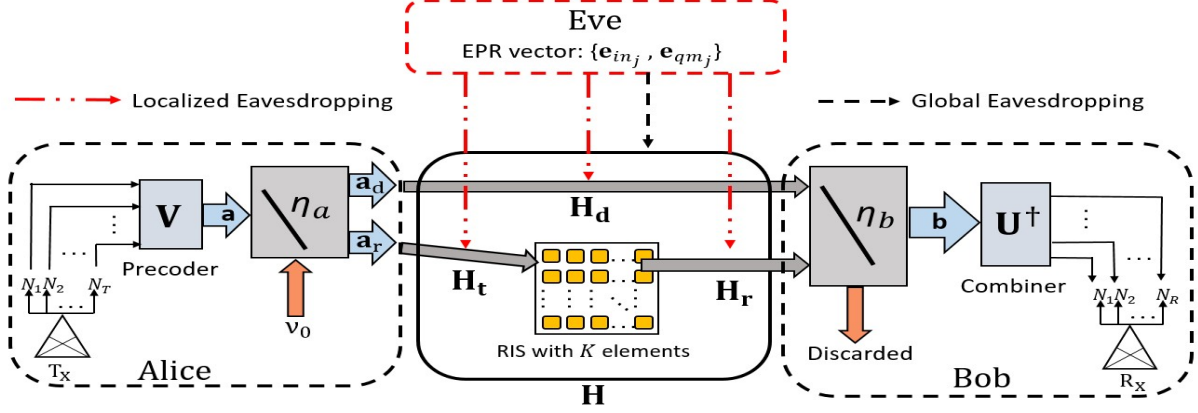


Fig. 1: The considered RIS-assisted MIMO CV-QKD wireless communication system model under eavesdropping attacks.

## II. SYSTEM AND CHANNEL MODELS

We consider an RIS-assisted MIMO CV-QKD system as shown in Fig. 1, where the transmitter, Alice, and the receiver, Bob, are equipped with  $N_T$  and  $N_R$  antennas, respectively. The RIS consists of  $K$  passive reflecting elements configured to adjust the phases of the incident and transmitted electromagnetic signals [15]. This communication is also aided by the direct LoS path between the transceiver pair.

### A. Channel Model

The effective MIMO channel between Alice and Bob, denoted by  $\mathbf{H} \in \mathbb{C}^{N_R \times N_T}$ , can be mathematically expressed as follows [16]:

$$\mathbf{H} \triangleq \mathbf{H}_d + \mathbf{H}_r \Phi \mathbf{H}_t, \quad (1)$$

where  $\Phi \triangleq \text{diag}(e^{j\phi_1}, \dots, e^{j\phi_K})$  and  $\phi_k$  is the phase shift introduced by the  $k$ -th element of the RIS. Furthermore,  $\mathbf{H}_d \in \mathbb{C}^{N_R \times N_T}$ ,  $\mathbf{H}_t \in \mathbb{C}^{K \times N_T}$ , and  $\mathbf{H}_r \in \mathbb{C}^{N_R \times K}$ , are the direct LoS channel matrix between the legitimate transceiver pair, the channel matrix between Alice and RIS, and the channel matrix between RIS and Bob, respectively, which are expressed for the THz system as follows:

$$\begin{aligned} \mathbf{H}_d &\triangleq \sum_{\ell=1}^{L_d} \sqrt{\delta_{d,\ell}} e^{j2\pi f_c \tau_{d,\ell}} \mathbf{h}_{N_R}(\theta_\ell^{R_X}) \mathbf{h}_{N_T}^\dagger(\theta_\ell^{T_X}), \\ \mathbf{H}_t &\triangleq \sum_{m=1}^{L_t} \sqrt{\delta_{g,m}} e^{j2\pi f_c \tau_{g,m}} \mathbf{h}_{\text{RIS}}(\varphi, \theta_m^{\text{RIS}}) \mathbf{h}_{N_T}^\dagger(\theta_m^{T_X}), \\ \mathbf{H}_r &\triangleq \sum_{n=1}^{L_r} \sqrt{\delta_{f,n}} e^{j2\pi f_c \tau_{f,n}} \mathbf{h}_{N_R}(\theta_n^{R_X}) \mathbf{h}_{\text{RIS}}^\dagger(\varphi, \theta_n^{\text{RIS}}). \end{aligned} \quad (2)$$

In these expressions,  $L_d$ ,  $L_t$ , and  $L_r$  denote the number of signal propagation paths in the wireless channels  $\mathbf{H}_d$ ,  $\mathbf{H}_t$ , and  $\mathbf{H}_r$ , respectively. Further,  $f_c$  is the carrier frequency, and  $\tau_d$ ,  $\tau_t$ ,  $\tau_r$  and  $\delta_d$ ,  $\delta_t$ ,  $\delta_r$  are the propagation delays and path losses corresponding to  $\mathbf{H}_d$ ,  $\mathbf{H}_t$ , and  $\mathbf{H}_r$ , respectively. Moreover,  $\theta_\ell^{T_X}$ ,  $\theta_m^{T_X}$ , and  $\theta_n^{\text{RIS}}$  are the angles of departure (AoD) and  $\theta_\ell^{R_X}$ ,  $\theta_m^{\text{RIS}}$ , and  $\theta_n^{R_X}$  are the angles of arrival (AoA) of the  $\ell$ -th,  $m$ -th, and  $n$ -th multipath from the transmitter's

and the receiver's uniform linear arrays (ULAs), respectively. The antenna elements in both ULAs are uniformly placed in a single dimension such that the inter-element spacing is maintained at  $d_a$ . This results in the array response vector in (2), i.e.,  $\mathbf{h}_{N_T}$  (or  $\mathbf{h}_{N_R}$ ), are given as follows:

$$\mathbf{h}_N(\theta) \triangleq \frac{1}{\sqrt{N}} \left[ 1, e^{j\frac{2\pi}{\lambda_c} d_a \sin \theta}, \dots, e^{j\frac{2\pi}{\lambda_c} d_a (N-1) \sin \theta} \right]^T, \quad (3)$$

where  $N \in \{N_T, N_R\}$  and  $\lambda_c \triangleq c/f_c$ , with  $c$  being the speed of electromagnetic signals (i.e., light). Furthermore,  $\mathbf{h}_{\text{RIS}} \in \mathbb{C}^{K \times 1}$  in (2) is the response vector of the passive ULA of the RIS [56], [57] and is given as

$$\begin{aligned} \mathbf{h}_{\text{RIS}}(\varphi, \theta_i^{\text{RIS}}) &= \frac{1}{\sqrt{K}} \left[ e^{j\frac{2\pi}{\lambda_c} (\vartheta_X^{\varphi, \theta_i^{\text{RIS}}} + \vartheta_Y^{\varphi, \theta_i^{\text{RIS}}})}, \dots \right. \\ &\quad \left. \dots, e^{j\frac{2\pi}{\lambda_c} ((K_X-1)\vartheta_X^{\varphi, \theta_i^{\text{RIS}}} + (K_Y-1)\vartheta_Y^{\varphi, \theta_i^{\text{RIS}}})} \right], \end{aligned} \quad (4)$$

where, for  $i \in \{m, n\}$ , it holds:

$$\begin{aligned} \vartheta_X^{\varphi, \theta_i^{\text{RIS}}} &= d_X \cos(\varphi) \sin(\theta_i^{\text{RIS}}), \\ \vartheta_Y^{\varphi, \theta_i^{\text{RIS}}} &= d_Y \sin(\varphi) \sin(\theta_i^{\text{RIS}}). \end{aligned} \quad (5)$$

Here, the elements of the RIS are considered to be arranged along a 2-dimensional structure [19], [58] with  $K_X$  and  $K_Y$  reflecting elements along the horizontal and the vertical axes, respectively, implying that  $K_X K_Y = K$ , with the separation between the elements in the corresponding axes being denoted by  $d_X$  and  $d_Y$ . Furthermore, the path losses in (2) are expressed as follows:

$$\delta_{j,i} = \begin{cases} \left(\frac{\lambda_c}{4\pi d_{j,i}}\right)^2 G_{T_X} G_{R_X} 10^{-0.1\rho d_{j,i}}, & j \in \{d, g, f\}, i = 1 \\ \varsigma \xi_i \left(\frac{\lambda_c}{4\pi d_{j,i}}\right)^2 G_{T_X} G_{R_X} 10^{-0.1\rho d_{j,i}}, & i \in \{\ell, m, n \neq 1\}, \end{cases} \quad (6)$$

where  $d_{j,i}$  is the smallest path length,  $\xi_i$  is the Fresnel reflection coefficient of the  $i$ -th multipath component,  $\varsigma$  is the Rayleigh roughness factor, and  $\rho$  (in dB/km) is the atmospheric absorption loss. Moreover, Alice's and Bob's ULAs gains are  $G_{T_X} = N_T G_a$  and  $G_{R_X} = N_R G_a$ , respectively, where  $G_a$  is the gain of each component of the transmitter and receiver

antennas, and  $G_{T_X}$  (or  $G_{R_X}$ ) =  $K$  when the data symbols are transmitted from (or to) the RIS, respectively.

### B. Secret Key Generation, Transmission, and Reception

In the considered MIMO wireless communication system, Alice aims to establish a secure quantum key with Bob. To this end, Alice employs a Gaussian-modulated CV-QKD scheme, generating two independent zero-mean Gaussian random vectors  $\mathbf{X}_{\text{Alice}}, \mathbf{P}_{\text{Alice}} \sim \mathcal{N}(\mathbf{0}_{N_T}, V_s \mathbf{I}_{N_T})$  corresponding to the position and momentum quadratures, respectively [50], [59]. Using these quadratures, Alice generates a set of coherent states,  $a_t = X_{\text{Alice},t} + jP_{\text{Alice},t}$ , for  $t = 1, \dots, N_T$ , which are transmitted to Bob through the wireless propagation medium. After propagation through the wireless medium, the received quantum signal at Bob is modeled as the coherent combination of the fields arriving through the direct and RIS-assisted paths. This operation is represented by a beam splitter ( $\text{BS}_b$ ) with transmissivity  $\eta_b$ , yielding the received quantum signal expression:

$$\hat{\mathbf{b}} \triangleq \sqrt{\eta_b} \hat{\mathbf{b}}_d + \sqrt{1 - \eta_b} \hat{\mathbf{b}}_r, \quad (7)$$

where  $\hat{\mathbf{b}}_d$  and  $\hat{\mathbf{b}}_r$  represent the signals arriving from the direct and RIS-assisted channels, respectively. The signal to the direct path and the RIS-assisted path are expressed as follows:

$$\hat{\mathbf{b}}_d \triangleq \mathbf{H}_d \hat{\mathbf{a}}_d + \mathbf{N}_d \hat{\mathbf{e}}_d, \quad (8a)$$

$$\hat{\mathbf{b}}_r \triangleq (\mathbf{H}_r \Phi \mathbf{H}_t) \hat{\mathbf{a}}_r + \mathbf{H}_r \Phi \mathbf{N}_t \hat{\mathbf{e}}_t + \mathbf{N}_r \hat{\mathbf{e}}_r, \quad (8b)$$

respectively, where  $\hat{\mathbf{e}}_d$ ,  $\hat{\mathbf{e}}_t$ , and  $\hat{\mathbf{e}}_r$  denote mutually independent bosonic environmental modes associated with losses along the direct path, the Alice-RIS path, and the RIS-Bob path, respectively, which follow  $[\hat{\mathbf{e}}_i, \hat{\mathbf{e}}_j^\dagger] = \delta_{i,j} \mathbf{I}_{N_j}$ ,  $\forall j \in \{d, t, r\}$ , and  $N_j \in \{\min(N_T, N_R), \min(N_T, K), \min(K, N_R)\}$ . To generate independent propagation modes for the direct and RIS-enabled channel paths, Alice first splits the transmitted signal using a beam splitter ( $\text{BS}_a$ ) with transmissivity  $\eta_a$  as follows:

$$\hat{\mathbf{a}}_d \triangleq \sqrt{\eta_a} \hat{\mathbf{a}} + \sqrt{1 - \eta_a} \hat{\mathbf{v}}_0, \quad (9a)$$

$$\hat{\mathbf{a}}_r \triangleq -\sqrt{1 - \eta_a} \hat{\mathbf{a}} + \sqrt{\eta_a} \hat{\mathbf{v}}_0, \quad (9b)$$

where  $\hat{\mathbf{v}}_0$  is a vacuum mode vector and  $\hat{\mathbf{a}}$  is the Alice transmitted mode vector. These operators satisfy the canonical bosonic commutation relations:

$$[\hat{\mathbf{a}}, \hat{\mathbf{a}}^\dagger] = \mathbf{I}_{N_T}, [\hat{\mathbf{v}}_0, \hat{\mathbf{v}}_0^\dagger] = \mathbf{I}_{N_T}, [\hat{\mathbf{a}}, \hat{\mathbf{v}}_0^\dagger] = \mathbf{0}_{N_T \times N_T}. \quad (10)$$

Furthermore, each propagation segment is modeled as a physically realizable Gaussian channel arising from a unitary interaction between the signal and the environment, which is given as  $\mathbf{H}_j \mathbf{H}_j^\dagger + \mathbf{N}_j \mathbf{N}_j^\dagger = \mathbf{I}_{N_j}$ ,  $\forall j \in \{d, t, r\}$ . Here,  $\mathbf{N}_j$  denotes the environmental coupling matrices which characterize the interaction between the signal and the corresponding environmental mode  $\hat{\mathbf{e}}_j$ ,  $\forall j \in \{d, t, r\}$ . Since the signal and environmental modes originate from a single global unitary transformation, the received operator  $\hat{\mathbf{b}}$  at Bob satisfies the canonical bosonic commutation relations:

$$[\hat{\mathbf{b}}, \hat{\mathbf{b}}^\dagger] = \mathbf{I}_{N_R}. \quad (11)$$

### C. Eavesdropping Models

As depicted in Fig. 1, Eve acts as an external adversary that is assumed to have unlimited computational and quantum processing capabilities, while remaining subject to the fundamental laws of quantum mechanics. Bob's receiver noise and internal imperfections are assumed to be trusted and inaccessible to Eve. On the other hand, Eve is assumed to perform collective Gaussian attacks against Gaussian-modulated CV-QKD protocols, which can be equivalently modeled as an entangling-cloner attack. In this model, Eve prepares two-mode squeezed vacuum (TMSV) states, also known as Einstein-Podolsky-Rosen (EPR) pairs, consisting of an injected mode and a retained idler mode [27]. The covariance matrix of a TMSV state is given by the following expression [47]:

$$\Sigma_{\text{EPR}} \triangleq \begin{bmatrix} \frac{V_e \mathbf{I}_2}{\sqrt{V_e^2 - 1}} & \sqrt{V_e^2 - 1} \mathbf{Z} \\ \sqrt{V_e^2 - 1} \mathbf{Z} & V_e \mathbf{I}_2 \end{bmatrix}, \quad (12)$$

where  $\mathbf{Z}$  is the Pauli-z matrix given as  $\text{diag}(1, -1)$  and  $V_e$  denotes the variance of Eve's EPR modes.

In an entangling-cloner attack, Eve injects one mode of a TMSV state into the environmental input of a lossy channel segment, while retaining the corresponding idler mode in their quantum memory. Consequently, the corresponding environmental output mode constitutes Eve's observation of the leaked signal. Based on Eve's control and observation over different segments of the system model, we consider hereinafter the following two eavesdropping scenarios.

#### 1) Localized Eavesdropping Based on Physical Access:

In the localized eavesdropping scenarios, Eve is assumed to be physically present along only one propagation segment of the communication link. As a result, they can access and manipulate only the environmental modes associated with loss on that specific segment, while all remaining environmental modes and Bob's receiver noise are considered trusted and inaccessible to Eve. Thus, we consider the following localized eavesdropping cases:

- **Eavesdropping on the Alice-Bob direct path ( $\mathbf{H}_d$ ):** Eve accesses the environmental mode  $\hat{\mathbf{e}}_d$  associated with loss on the direct Alice-Bob link, while the losses via the RIS-assisted propagation remain inaccessible.
- **Eavesdropping on the Alice-RIS path ( $\mathbf{H}_t$ ):** Eve accesses the environmental mode  $\hat{\mathbf{e}}_t$  corresponding to the loss between Alice and the RIS.
- **Eavesdropping on the RIS-Bob path ( $\mathbf{H}_r$ ):** Eve accesses the environmental mode  $\hat{\mathbf{e}}_r$  associated with loss on the RIS-Bob segment.

In all the above cases, Eve's interaction with the channel is restricted to a single lossy propagation segment. The remaining loss mechanisms are modeled as trusted vacuum noise.

2) *Global Eavesdropping via Effective Channel Purification:* While localized eavesdropping represents realistic physical limitations on Eve's access, it is essential in the security analysis of CV-QKD to adopt a more rigorous approach. In this global eavesdropping scenario, Eve has full control over purifying the effective end-to-end channel between Alice and Bob. Since any lossy Gaussian channel can be modeled as a

beam splitter interaction with a vacuum-state environment, the overall channel comprising the direct path  $\mathbf{H}_d$  and the RIS-assisted path (i.e.,  $\mathbf{H}_t$  followed by  $\mathbf{H}_r$ ) can be equivalently described by a single effective transmissivity  $\beta$ . Eve is then assumed to control the environmental input corresponding to this effective channel, injecting one mode of a TMSV state and retaining the idler in their quantum memory.

### III. SECRET KEY RATE ANALYSIS

The SKR in QKD quantifies the number of information-theoretically secure key bits that Alice and Bob can extract per channel use, accounting for the maximum information an eavesdropper can obtain under a given attack model. In this work, the physical channel model remains fixed as described in Section II, while different eavesdropping scenarios are distinguished by Eve's access to the environmental modes associated with channel loss, as outlined in Section III.

We consider that Alice and Bob have perfect channel state information (CSI) [1], [54]. Let  $\mathbf{H} = \mathbf{U}\mathbf{D}\mathbf{V}^\dagger$  be the singular value decomposition (SVD) of the overall channel  $\mathbf{H}$ . Thus, with the intention of maximizing the data rate, Alice employs the precoder matrix as  $\mathbf{V}$  before passing to the BS<sub>a</sub>, and Bob employs its combiner as  $\mathbf{U}^\dagger$  to one of output of the BS<sub>b</sub>. Following the transmission of keys from Alice and the interaction with environmental modes, Bob receives the signal and performs measurements to decrypt the secret keys. In this context, Bob can perform two types of measurements, as follows: 1) homodyne, where he measures one of the two quadratures randomly, and 2) heterodyne, where he measures both quadratures simultaneously [59], [60]. Previous studies indicate that both homodyne and heterodyne measurements yield similar results due to increased detector noise in heterodyne measurements [54]. Therefore, we consider that Bob performs homodyne measurements. Consequently, the output vector at Bob is given as

$$\begin{aligned} \mathbf{b} = & \mathbf{U}^\dagger \left( \sqrt{\eta_a \eta_b} \mathbf{H}_d - \sqrt{(1-\eta_a)(1-\eta_b)} \mathbf{H}_r \Phi \mathbf{H}_t \right) \mathbf{V}_a \\ & + \mathbf{U}^\dagger \left( \sqrt{(1-\eta_a)\eta_b} \mathbf{H}_d + \sqrt{\eta_a(1-\eta_b)} \mathbf{H}_r \Phi \mathbf{H}_t \right) \mathbf{v}_0 \\ & + \sqrt{\eta_b} \mathbf{U}^\dagger \mathbf{N}_d \mathbf{e}_d + \sqrt{1-\eta_b} \mathbf{U}^\dagger \mathbf{H}_r \Phi \mathbf{N}_t \mathbf{e}_t \\ & + \sqrt{1-\eta_b} \mathbf{U}^\dagger \mathbf{N}_r \mathbf{e}_r + \mathbf{U}^\dagger \mathbf{n}_b. \end{aligned} \quad (13)$$

Following the homodyne measurement, a reconciliation technique is employed by Bob to fix errors, which are typically of two types, namely, 1) direct reconciliation (DR) and 2) RR [50], [61]. RR works better than DR because the RR protocol can achieve positive SKR for any values of transmittance between 0 and 1, while DR needs more than 50% of the transmittance value to achieve a positive SKR. Owing to this reason, we consider Bob to employ the RR protocol.

#### A. Localized Eavesdropping Based on Physical Access

Taking into account the homodyne measurement and RR at Bob's end, as well as Eve's eavesdropping models described in Section III.A, the secret key rate is given as

$$\text{SKR}_j = \mathcal{I}(A; B) - \chi_j(B; E_j), \quad j \in \{d, t, r\}, \quad (14)$$

where  $\mathcal{I}(A; B)$  denotes the classical mutual information between Alice and Bob, and  $\chi_j(B; E_j)$  represents the Holevo (quantum) information of Bob's and Eve's quantum states from the  $j$ -th link. The achievable mutual information between Alice and Bob is given as

$$\mathcal{I}(A; B) = \mathcal{H}(B) - \mathcal{H}(B|A), \quad (15)$$

where  $\mathcal{H}(B)$  is the Shannon entropy, expressed as

$$\mathcal{H}(B) = - \int_{\mathbb{C}^{N_R}} f(\mathbf{b}) \log_2(f(\mathbf{b})), \quad (16)$$

and  $\mathcal{H}(B|A)$  is the conditional Shannon entropy computed as

$$\mathcal{H}(B|A) = - \int_{\mathbb{C}^{N_R}} f(\mathbf{b}|\mathbf{a}) \log_2(f(\mathbf{b}|\mathbf{a})). \quad (17)$$

Here,  $f(\mathbf{b})$  and  $f(\mathbf{b}|\mathbf{a})$  represent the probability density functions (p.d.f.s) of the vector  $\mathbf{b}$  and the conditional p.d.f. of  $\mathbf{b}$  given  $\mathbf{a}$ , respectively, which can be computed from (13). It is important to note that calculating these p.d.f.s requires the corresponding covariance matrices  $\Sigma_{\mathbf{b}}$  and  $\Sigma_{\mathbf{b}|\mathbf{a}}$ , which are obtained as

$$\begin{aligned} \Sigma_{\mathbf{b}} = & V_a \mathbf{U}^\dagger \left( \sqrt{\eta_a \eta_b} \mathbf{H}_d - \sqrt{(1-\eta_a)(1-\eta_b)} \mathbf{H}_r \Phi \mathbf{H}_t \right) \\ & \times \left( \sqrt{\eta_a \eta_b} \mathbf{H}_d - \sqrt{(1-\eta_a)(1-\eta_b)} \mathbf{H}_r \Phi \mathbf{H}_t \right)^\dagger \mathbf{U} \\ & + V_{v_0} \left( \sqrt{(1-\eta_a)\eta_b} \mathbf{H}_d + \sqrt{\eta_a(1-\eta_b)} \mathbf{H}_r \Phi \mathbf{H}_t \right) \\ & \times \left( \sqrt{(1-\eta_a)\eta_b} \mathbf{H}_d + \sqrt{\eta_a(1-\eta_b)} \mathbf{H}_r \Phi \mathbf{H}_t \right)^\dagger \\ & + V_{e_d} \eta_b \mathbf{U}^\dagger \mathbf{N}_d \mathbf{N}_d^\dagger \mathbf{U} + V_{e_r} (1-\eta_b) \mathbf{U}^\dagger \mathbf{N}_r \mathbf{N}_r^\dagger \mathbf{U} \\ & + V_{e_t} (1-\eta_b) \mathbf{U}^\dagger \mathbf{H}_r \Phi \mathbf{N}_t \mathbf{N}_t^\dagger \Phi^\dagger \mathbf{H}_r^\dagger \mathbf{U} + \sigma_b^2 \mathbf{I}_N, \end{aligned} \quad (18)$$

and

$$\begin{aligned} \Sigma_{\mathbf{b}|\mathbf{a}} = & V_0 \mathbf{U}^\dagger \left( \sqrt{\eta_a \eta_b} \mathbf{H}_d - \sqrt{(1-\eta_a)(1-\eta_b)} \mathbf{H}_r \Phi \mathbf{H}_t \right) \\ & \times \left( \sqrt{\eta_a \eta_b} \mathbf{H}_d - \sqrt{(1-\eta_a)(1-\eta_b)} \mathbf{H}_r \Phi \mathbf{H}_t \right)^\dagger \mathbf{U} \\ & + V_{v_0} \left( \sqrt{(1-\eta_a)\eta_b} \mathbf{H}_d + \sqrt{\eta_a(1-\eta_b)} \mathbf{H}_r \Phi \mathbf{H}_t \right) \\ & \times \left( \sqrt{(1-\eta_a)\eta_b} \mathbf{H}_d + \sqrt{\eta_a(1-\eta_b)} \mathbf{H}_r \Phi \mathbf{H}_t \right)^\dagger \\ & + V_{e_d} \eta_b \mathbf{U}^\dagger \mathbf{N}_d \mathbf{N}_d^\dagger \mathbf{U} + V_{e_t} (1-\eta_b) \mathbf{U}^\dagger \mathbf{N}_t \mathbf{N}_t^\dagger \mathbf{U} \\ & + V_{e_r} (1-\eta_b) \mathbf{U}^\dagger \mathbf{N}_r \mathbf{N}_r^\dagger \mathbf{U} + \sigma_b^2 \mathbf{I}_N, \end{aligned} \quad (19)$$

where  $N = \min\{N_T, N_R, K\}$ ,  $V_a = (V_s + V_0)$ ,  $V_s$  is the variance of Alice signal state and  $V_0$  represents the variance of the preparation vacuum state,  $V_{v_0}$  denotes the variance of the vacuum state  $v_0$  at BS<sub>a</sub>, and  $V_{e_j}$  is the variance of the environmental mode associated with segment  $j$ . Using (15)-(19) followed by algebraic simplifications, the mutual information in (14) is obtained as

$$\mathcal{I}(A; B) = \frac{1}{2} \log_2 \left| \frac{\Sigma_{\mathbf{b}}}{\Sigma_{\mathbf{b}|\mathbf{a}}} \right|. \quad (20)$$

On another front, for a given eavesdropping scenario on segment  $j \in \{d, t, r\}$ , Eve is assumed to access only the environmental mode associated with that segment. Specifically, Eve prepares the environmental input mode  $\hat{\mathbf{e}}_{in_j}$  of a TMSV

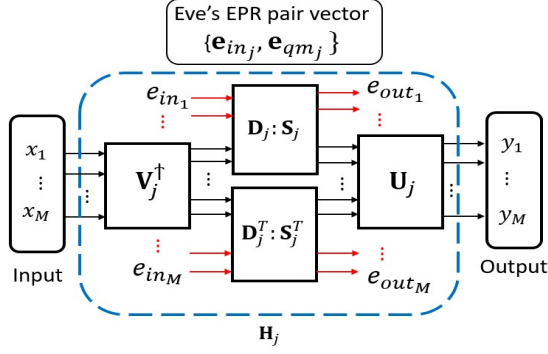


Fig. 2: A depiction of four beam-splitter models representing Eve's attack model for the considered MIMO channel.

state with variance  $V_{e_j}$ , while retaining the other modes  $\hat{\mathbf{e}}_{\text{qm},j}$  in their quantum memory. All remaining environmental modes are assumed to be in the vacuum state. The environmental output modes available to Eve by modeling a lossy channel with the BSs as depicted in Fig. 2, are given as

$$\mathbf{e}_{\text{out},j} = \begin{cases} -\sqrt{\eta_a} \mathbf{S}_d \mathbf{V}_d^\dagger \mathbf{V}_a + \sqrt{(1-\eta_a)} \mathbf{S}_d \mathbf{V}_d^\dagger \mathbf{v}_0 + \mathbf{D}_d \mathbf{e}_{\text{in}_d} & , j = d, \\ -\sqrt{(1-\eta_a)} \mathbf{S}_t \mathbf{V}_t^\dagger \mathbf{V}_a + \sqrt{\eta_a} \mathbf{S}_t \mathbf{V}_t^\dagger \mathbf{v}_0 + \mathbf{D}_t \mathbf{e}_{\text{in}_t} & , j = t, \\ -\sqrt{(1-\eta_a)} \mathbf{S}_r \mathbf{V}_r^\dagger \Phi \mathbf{H}_t \mathbf{V}_a + \sqrt{\eta_a} \mathbf{S}_r \mathbf{V}_r^\dagger \Phi \mathbf{H}_t \mathbf{v}_0 \\ -\mathbf{S}_r \mathbf{V}_r^\dagger \Phi \mathbf{U}_t \mathbf{S}_t \mathbf{e}_{\text{in}_t} + \mathbf{D}_r \mathbf{e}_{\text{in}_r} & , j = r, \end{cases} \quad (21)$$

where matrix  $\mathbf{D}_j$  and  $\mathbf{S}_j$  are given as

$$\mathbf{D}_j = \begin{bmatrix} \text{diag}(\sqrt{\beta_{j,1}}, \dots, \sqrt{\beta_{j,r_H}}) & \mathbf{0}_{r_H \times (N_j - r_H)} \\ \mathbf{0}_{(N_j - r_H) \times r_H} & \mathbf{0}_{(N_j - r_H) \times (N_j - r_H)} \end{bmatrix}, \quad (22a)$$

and

$$\mathbf{S}_j = \text{diag} \left( \sqrt{1 - \beta_{j,1}}, \dots, \sqrt{1 - \beta_{j,r_H}}, \underbrace{1, \dots, 1}_{(N_j - r_H) \text{ times}} \right), \quad (22b)$$

where  $\sqrt{\beta_{j,1}}, \dots, \sqrt{\beta_{j,r_H}}$  are the  $r_H$  non-zero singular values of the  $j$ -th channel matrix. Consequently the environmental coupling matrices  $\mathbf{N}_j$  for the corresponding channel are given as

$$\mathbf{N}_j = \mathbf{U}_j \mathbf{S}_j, \quad j \in \{d, t, r\}. \quad (23)$$

The Holevo information between Bob and Eve for the localized eavesdropping scenario on segment  $j$  is given by

$$\chi_j(B; E_j) = \mathcal{S}(E_j) - \mathcal{S}(E_j|B), \quad (24)$$

where  $\mathcal{S}(E_j)$  and  $\mathcal{S}(E_j|B)$  represent the von Neumann (quantum) entropy of Eve's modes and the conditional von Neumann entropy of Eve's modes given Bob's received modes. These are found by calculating the symplectic eigenvalues  $\{\lambda_{E_j}\}_{i=1}^N$  and  $\{\lambda_{E_j|B}\}_{i=1}^N$  of their corresponding correlation matrices,  $\Sigma_{E_j}$  and  $\Sigma_{E_j|B}$ , respectively. The von Neumann entropy is computed as

$$\mathcal{S}(E_j) \text{ (or) } \mathcal{S}(E_j|B) = \sum_{i=1}^{N_j} h_o(\lambda_j), \quad (25)$$

where  $\lambda_j \geq 1$  are the symplectic eigenvalues of the correlation matrices, and the function  $h_o(\cdot)$  is given as

$$h_o(\lambda) = \left( \frac{\lambda+1}{2} \right) \log_2 \left( \frac{\lambda+1}{2} \right) - \left( \frac{\lambda-1}{2} \right) \log_2 \left( \frac{\lambda-1}{2} \right). \quad (26)$$

Moreover, Eve's correlation matrix for  $j \in \{d, t, r\}$ , denoted as  $\Sigma_{E_j}$ , is generated from two components of the received vector at Eve's end. For a given eavesdropping scenario  $j$ , Eve's accessible quantum system consists of the environmental output mode  $\mathbf{e}_{\text{out}_j}$  and the retained idler mode  $\mathbf{e}_{\text{qm}_j}$ . The corresponding covariance matrix is given as

$$\Sigma_{E_j} = \begin{bmatrix} \Sigma_{\mathbf{e}_{\text{out}_j}} & \Sigma_{\mathbf{e}_{\text{out}_j} \mathbf{e}_{\text{qm}_j}} \\ \Sigma_{\mathbf{e}_{\text{qm}_j} \mathbf{e}_{\text{out}_j}} & \Sigma_{\mathbf{e}_{\text{qm}_j}} \end{bmatrix}, \quad j \in \{d, t, r\}, \quad (27)$$

where  $\Sigma_{\mathbf{e}_{\text{qm}_j}} = V_{e_j} \mathbf{I}_{N_j}$ ,  $\Sigma_{\mathbf{e}_{\text{out}_j}} = \sqrt{V_{e_j}^2 - 1} \mathbf{D}_j$ ,  $j \in \{d, t, r\}$ , and

$$\Sigma_{\mathbf{e}_{\text{out}_j}} = \begin{cases} \eta_a V_a \mathbf{S}_d \mathbf{S}_d^\dagger + (1-\eta_a) V_{v_0} \mathbf{S}_d \mathbf{S}_d^\dagger + V_{e_d} \mathbf{D}_d \mathbf{D}_d^\dagger & , j = d, \\ (1-\eta_a) V_a \mathbf{S}_t \mathbf{S}_t^\dagger + \eta_a V_{v_0} \mathbf{S}_t \mathbf{S}_t^\dagger + V_{e_t} \mathbf{D}_t \mathbf{D}_t^\dagger & , j = t, \\ ((1-\eta_a) V_a + \eta_a V_{v_0}) (\mathbf{S}_r \mathbf{V}_r^\dagger \Phi \mathbf{H}_t) (\mathbf{S}_r \mathbf{V}_r^\dagger \Phi \mathbf{H}_t)^\dagger + \\ V_{e_t} (\mathbf{S}_r \mathbf{V}_r^\dagger \Phi \mathbf{U}_t \mathbf{S}_t) (\mathbf{S}_r \mathbf{V}_r^\dagger \Phi \mathbf{U}_t \mathbf{S}_t)^\dagger + V_{e_r} \mathbf{D}_r \mathbf{D}_r^\dagger & , j = r. \end{cases} \quad (28)$$

Furthermore, Eve's conditional von Neumann entropy  $\mathcal{S}(E_j|B)$  is obtained from the correlation matrix generated with the  $\mathbf{b}$ ,  $\mathbf{e}_{\text{out}_j}$ , and  $\mathbf{e}_{\text{qm}_j}$  is given as

$$\Sigma_{E_j|B} = \begin{bmatrix} \Sigma_{E_j} & \Sigma_{E_j B} \\ \Sigma_{E_j B}^\dagger & \Sigma_{\mathbf{b}} \end{bmatrix}, \quad j \in \{d, t, r\}. \quad (29)$$

This leads to the conditional covariance matrix of Eve's modes that are dependent on the outcomes of Bob's homodyne measurements, which is represented as

$$\Sigma_{E_j|B} = \Sigma_{E_j} - \Sigma_{E_j B} (\Pi (\Sigma_{\mathbf{b}} \otimes \mathbf{I}_2) \Pi) \Pi^{-1*} \Sigma_{E_j B}^\dagger, \quad (30)$$

where  $\Pi = \mathbf{I}_{N_j} \otimes \begin{pmatrix} 1 & 0 \\ 0 & 0 \end{pmatrix}$ , and  $\Sigma_{\mathbf{b}}$  and  $\Sigma_{E_j}$  are given in (18) and (27), respectively. Furthermore,  $\Sigma_{E_j B}$  is the quantum correlation of Eve's received mode  $\mathbf{e}_{\text{out}_j}$  and Eve's stored mode in quantum memory  $\mathbf{e}_{\text{qm}_j}$  with Bob's output modes  $\mathbf{b}$  is given as

$$\Sigma_{E_j B} = \begin{bmatrix} \Sigma_{\mathbf{e}_{\text{out}_j} \mathbf{b}} \\ \Sigma_{\mathbf{e}_{\text{qm}_j} \mathbf{b}} \end{bmatrix}, \quad j \in \{d, t, r\}, \quad (31)$$

where  $\Sigma_{\mathbf{e}_{\text{out}_j} \mathbf{b}}$  is given in (32) on the top of the next page, and

$$\Sigma_{\mathbf{e}_{\text{qm}_j} \mathbf{b}} = \begin{cases} \sqrt{\eta_b} \sqrt{V_{e_d}^2 - 1} (\mathbf{U}^\dagger \mathbf{U}_d \mathbf{S}_d)^\dagger & , j = d, \\ \sqrt{(1-\eta_b)} \sqrt{V_{e_t}^2 - 1} (\mathbf{U}^\dagger \mathbf{H}_r \Phi \mathbf{U}_t \mathbf{S}_t)^\dagger & , j = t, \\ \sqrt{(1-\eta_b)} \sqrt{V_{e_r}^2 - 1} (\mathbf{U}^\dagger \mathbf{U}_r \mathbf{S}_r)^\dagger & , j = r. \end{cases} \quad (32)$$

Using (20) and (25), the SKR for RIS-assisted MIMO CV-QKD under the considered Eavesdropping model is given in (34) on the top of the next page.

$$\Sigma_{e_{o_j}, b} = \begin{cases} -\sqrt{\eta_b}(\eta_a V_a + (1 - \eta_a) V_{v_0}) \mathbf{S}_d \mathbf{V}_d^\dagger \mathbf{H}_d^\dagger \mathbf{U} + \sqrt{\eta_b} V_{e_d} \mathbf{D}_d \mathbf{S}_d^\dagger \mathbf{U}_d^\dagger \mathbf{U} \\ -\sqrt{\eta_a(1 - \eta_a)(1 - \eta_b)}(V_a - V_{v_0}) \mathbf{S}_d \mathbf{V}_d^\dagger (\mathbf{H}_r \Phi \mathbf{H}_t)^\dagger \mathbf{U} & , j = d, \\ \sqrt{\eta_a \eta_b (1 - \eta_a)}(V_{v_0} - V_a) \mathbf{S}_t \mathbf{V}_t^\dagger \mathbf{H}_d^\dagger \mathbf{U} + \sqrt{(1 - \eta_b)} V_{e_t} \mathbf{D}_t \mathbf{S}_t^\dagger \mathbf{U}_t^\dagger \Phi^\dagger \mathbf{H}_r^\dagger \mathbf{U} \\ + \sqrt{(1 - \eta_b)}((1 - \eta_a) V_a + \eta_a V_{v_0}) \mathbf{S}_t \mathbf{V}_t^\dagger (\mathbf{H}_r \Phi \mathbf{H}_t)^\dagger \mathbf{U} & , j = t, \\ \sqrt{\eta_a \eta_b (1 - \eta_a)}(V_{v_0} - V_a) \mathbf{S}_r \mathbf{V}_r^\dagger \Phi \mathbf{H}_t \mathbf{H}_d^\dagger \mathbf{U} - \sqrt{(1 - \eta_b)} V_{e_r} \mathbf{S}_r \mathbf{V}_r^\dagger \Phi \mathbf{U}_t \mathbf{S}_t \mathbf{S}_t^\dagger \mathbf{U}_t^\dagger \Phi^\dagger \mathbf{H}_r^\dagger \mathbf{U} \\ + \sqrt{(1 - \eta_b)}((1 - \eta_a) V_a + \eta_a V_{v_0}) \mathbf{S}_r \mathbf{V}_r^\dagger \Phi \mathbf{H}_t (\mathbf{H}_r \Phi \mathbf{H}_t)^\dagger \mathbf{U} + \sqrt{(1 - \eta_b)} V_{e_r} \mathbf{D}_r \mathbf{S}_r^\dagger \mathbf{U}_r^\dagger \mathbf{U} & , j = r \end{cases} \quad (32)$$

$$\text{SKR}_j = \frac{1}{2} \log_2 \left| \mathbf{I}_N + V_s \mathbf{U}^\dagger \left( \sqrt{\eta_a \eta_b} \mathbf{H}_d - \sqrt{(1 - \eta_a)(1 - \eta_b)} \mathbf{H}_r \Phi \mathbf{H}_t \right) \left( \sqrt{\eta_a \eta_b} \mathbf{H}_d - \sqrt{(1 - \eta_a)(1 - \eta_b)} \mathbf{H}_r \Phi \mathbf{H}_t \right)^\dagger \mathbf{U} \right. \\ \left. \times (\Sigma_{\mathbf{b}|\mathbf{a}})^{-1} \right| - \left( \sum_{i=1}^{N_j} h_o(\lambda_{E_j, i}) - \sum_{i=1}^{N_j} h_o(\lambda_{E_j|B, i}) \right), \quad j \in \{d, t, r\} \quad (34)$$

### B. Global Eavesdropping via Effective Channel Purification

In addition to the localized eavesdropping scenarios considered in the previous subsections, we now examine a benchmark case in which Eve is assumed to have access to the purification of the entire effective channel between Alice and Bob. This model corresponds to a collective Gaussian attack on the overall channel.

In this setting, Eve is assumed to have full knowledge of the overall channel matrix  $\mathbf{H}$ , including perfect CSI. By employing the SVD and following standard CV-QKD analysis, Alice applies the precoder  $\mathbf{V}$  and Bob applies the combiner  $\mathbf{U}^\dagger$ , thereby transforming the system into  $r_H$  equivalent SISO channels. Consequently, the input-output relations for the  $i$ -th parallel channel are given by

$$b_i = \sqrt{\beta_i} \psi_i + \sqrt{1 - \beta_i} e_{in_i} + n_{b_i}, \quad (35)$$

and

$$e_{o_i} = -\sqrt{1 - \beta_i} \psi_i + \sqrt{\beta_i} e_{in_i}, \quad (36)$$

where  $\sqrt{\beta_i} \forall i = 1, \dots, r_H$  are the singular values of  $\mathbf{H}$ , with  $r_H = \text{rank}(\mathbf{H})$ . Furthermore,  $e_{in_i}$  is one mode of Eve's TMSV state with variance  $V_e$ ,  $e_{o_i}$  is the corresponding environmental output mode accessible to Eve, and  $n_{b_i}$  represents trusted Gaussian noise at Bob.

Consequently, the expression for the SKR under the scenario where Eve employs a collective Gaussian entanglement attack on the overall channel, and considering RR, is given as

$$\text{SKR}_i = \mathcal{I}(A_i; B_i) - \chi(B_i; E_i), \quad (37)$$

where  $\mathcal{I}(A_i; B_i)$  is given by

$$\mathcal{I}(A_i; B_i) = \frac{1}{2} \log_2 \left( 1 + \frac{\beta_i V_s}{\beta_i V_0 + (1 - \beta_i) V_e + \sigma_b^2} \right), \quad (38)$$

where  $V_0$  is the vacuum noise variance,  $V_e$  is the variance of Eve's TMSV modes, and  $\sigma_b^2$  denotes the trusted receiver noise variance at Bob.

Similarly, the mutual quantum information  $\chi(B_i; E_i)$  [61], is expressed as

$$\chi(B_i; E_i) = S(E_i) - S(E_i|B_i), \quad (39)$$

where  $S(\cdot)$  denotes the von Neumann entropy. For the Gaussian state  $\{e_{o_i}, e_{qm_i}\}$  stored in Eve's quantum memory, the

corresponding covariance matrix  $\Sigma_{E_i}$  for each  $i$ -th parallel channel is expressed as

$$\Sigma_{E_i} = \begin{bmatrix} V_{e_{o_i}} \mathbf{I}_2 & V_{e_{o_i} e_{qm_i}} \mathbf{Z} \\ V_{e_{o_i} e_{qm_i}} \mathbf{Z}^T & V_e \mathbf{I}_2 \end{bmatrix}, \quad (40)$$

where  $V_{e_{o_i}} = (1 - \beta_i) V_a + \beta_i V_e$  and  $V_{e_{o_i} e_{qm_i}} = \sqrt{\beta_i (V_e^2 - 1)}$ . This results in the symplectic eigenvalues of the covariance matrix of Eve's ancillary modes being given as [61]

$$\lambda_{i,1,2} = \sqrt{\frac{1}{2} \left( \nabla_i \pm \sqrt{\nabla_i^2 - 4 \det(\Sigma_{E_i})} \right)}, \quad (41)$$

where

$$\nabla_i = V_{e_{o_i}}^2 + V_e^2 - 2\beta_i (V_e^2 - 1), \quad (42a)$$

and

$$\det(\Sigma_{E_i}) = (V_{e_{o_i}} V_e - \beta_i (V_e^2 - 1))^2. \quad (42b)$$

Similarly, the conditional covariance matrix of Eve's state given Bob's quadrature,  $\Sigma_{E_i|B_i}$ , is defined as follows [61]:

$$\Sigma_{E_i|B_i} \triangleq \Sigma_{E_i} - \frac{1}{V_{b_i}} \mathbf{W}_i \mathbf{M} \mathbf{W}_i^\dagger, \quad (43)$$

where  $\Sigma_{E_i}$  is given in (35) and

$$\mathbf{M} = \begin{bmatrix} 1 & 0 \\ 0 & 0 \end{bmatrix}, \quad \mathbf{W}_i = \begin{bmatrix} \langle E_{o_i} \cdot b_i \rangle \mathbf{I}_2 \\ \langle e_{qm_i} \cdot b_i \rangle \mathbf{Z} \end{bmatrix}. \quad (44)$$

From (39) and (40), we observe that  $\Sigma_{E_i|B_i}$  can be expressed in the form

$$\Sigma_{E_i|B_i} = \begin{bmatrix} \mathbf{A}_i & \mathbf{C}_i \\ \mathbf{C}_i^\dagger & \mathbf{B}_i \end{bmatrix}, \quad (45)$$

which is in a similar form as (40) where

$$\mathbf{A}_i = \text{diag} \left( \frac{V_a V_e + \sigma_b^2 V_{e_{o_i}}}{V_{b_i}}, V_{e_{o_i}} \right), \\ \mathbf{B}_i = \text{diag} \left( \frac{(1 - \beta_i + (\beta_i V_a + \sigma_b^2) V_e)}{V_{b_i}}, V_e \right), \\ \mathbf{C}_i = \text{diag} \left( \frac{(V_a + \sigma_b^2) V_{e_{o_i} e_{qm_i}}}{V_{b_i}}, -V_{e_{o_i} e_{qm_i}} \right). \quad (46)$$

Thus, the symplectic eigenvalues of the conditional covariance matrix can be calculated as:

$$\lambda_{i3,4} = \sqrt{\frac{1}{2} \left( \tilde{\nabla}_i \pm \sqrt{\tilde{\nabla}_i^2 - 4\det(\Sigma_{E_i|B_i})} \right)}, \quad (47)$$

where

$$\begin{aligned} \tilde{\nabla}_i &= \det(\mathbf{A}_i) + \det(\mathbf{B}_i) - 2\det(\mathbf{C}_i) \\ &= \frac{(1 - \beta_i) V_e (V_a^2 + 1) + 2\beta_i V_a}{V_{b_i}} + \sigma_b^2 \nabla_i, \end{aligned} \quad (48a)$$

and

$$\begin{aligned} \det(\Sigma_{E_i|B_i}) &= \det(\Sigma_{E_i}) \\ &+ \frac{\sigma_B^2 \Lambda(V_a V_e, 1) (\Xi + \Lambda(V_a V_e, 1) \sigma_b^2)}{V_{b_i}^2}, \end{aligned} \quad (48b)$$

where  $\Lambda(V_a V_e, 1) = (1 - \beta_i) V_a V_e + \beta_i$  and  $\Xi = \Lambda(1, V_a V_e) V_{e_{o_i}} + V_a V_e^2 - 2V_a V_{e_{o_i}}^2 e_{am_i}$ . Substituting all these results into (37) and performing algebraic simplifications leads to the expression for the effective SKR of the RIS-assisted MIMO CV-QKD, where Eve performs a collective Gaussian attack on the overall channel, which is given in (49) at the top of the next page.

### C. PSO-Based Joint RIS and Beam Splitters Optimization

In alignment with the proposed RIS-assisted MIMO CV-QKD system and the analytically derived SKR expressions accounting for localized and overall eavesdropping, the phase shifts of the RIS unit elements and values of  $\eta_a$  and  $\eta_b$  are optimized to enhance the system's secrecy performance. The goal of the optimization is to maximize the MIMO SKR by jointly adjusting the RIS phase shifts,  $\eta_a$  and  $\eta_b$ , within their feasible ranges. Mathematically, the objective function is given as

$$\begin{aligned} \mathcal{OP} : \max_{\Phi, \eta_a, \eta_b} & \text{SKR}_{\{d, t, r, \text{MIMO}\}} \\ \text{s.t.} & -\pi \leq \phi_k \leq \pi, \forall k \in \{1, \dots, K\}, \\ & \text{s.t. } 0 \leq \eta_a \leq 1 \text{ and } 0 \leq \eta_b \leq 1. \end{aligned} \quad (50)$$

Due to the highly nonlinear relationship between the SKR and the RIS phase matrix in the scenarios outlined in (34) and (49), a PSO-based algorithm (Algorithm 1) is used to solve the optimization problem presented in (50). This approach aims to determine the optimal configurations of the RIS phases and the optimal  $\eta_a$  and  $\eta_b$ , which are subsequently used to maximize the SKR.

## IV. NUMERICAL RESULTS AND DISCUSSION

This section presents the numerical results corroborating the analytical framework described and derived in the paper. For the simulation studies, we consider the standard system parameters as  $\rho = 50$  dB/Km,  $T_e = 296$  K (denoting the room temperature), antenna gain  $G_a = 30$  dBi,  $\sigma_b^2 = 0.01$ , the variance of Alice's initial modulated signal  $V_s = 1000$ , the variance of the vacuum state  $V_0 = 2\bar{n} + 1$  with  $\bar{n} = [\exp(hf_c/k_B T_e) - 1]^{-1}$ , where  $h$  is the plank's constant and  $k_B$  is the Boltzmann's constant, the variance of Alice's

---

### Algorithm 1 PSO-Based $\Phi$ , $\eta_a$ , and $\eta_b$ Joint Optimization

---

- 1: **Inputs:**  $N_T$ ,  $N_R$ , number of RIS elements  $K$ , transmission distance, and PSO configuration parameters.
  - 2: Specify the feasible search space for RIS phases as  $-\pi \leq \phi_k \leq \pi$ ,  $\forall k \in \{1, \dots, K\}$ , and  $0 \leq \eta_a, \eta_b \leq 1$ .
  - 3: **for** each considered transmission distance **do**
  - 4:   Generate the channel matrices  $\mathbf{H}_d$ ,  $\mathbf{H}_t$ ,  $\mathbf{H}_r$ , and  $\mathbf{H}$  using (2).
  - 5:   Define the fitness function as the SKR,  $\text{SKR}_{\{d, t, r, \text{MIMO}\}}$ .
  - 6:   Randomly initialize the particle swarm with random RIS phase configurations,  $\eta_a$ , and  $\eta_b$ .
  - 7:   **for** each PSO iteration **do**
  - 8:     Compute the fitness value  $\text{SKR}_{\{d, t, r, \text{MIMO}\}}$  for every particle.
  - 9:     Update the personal-best and global-best solutions based on the maximum fitness achieved.
  - 10:    Modify particle velocities and positions according to PSO update rules.
  - 11:    Project updated phase,  $\eta_a$ , and  $\eta_b$  values onto the feasible region defined in Step 2.
  - 12:    **end for**
  - 13:    Obtain the optimized RIS phase matrix  $\Phi_{\text{opt}}$ ,  $\eta_a$ , and  $\eta_b$ .
  - 14:    Evaluate the corresponding  $\text{SKR}_{\{d, t, r, \text{MIMO}\}}^{\text{max}}$ .
  - 15: **end for**
- 

quadrature  $V_a = V_s + V_0$ ,  $V_{v_0} = 1$ , and the variance of Eve's quadrature  $V_{e_j} = 1$ ,  $j \in \{d, t, r\}$  &  $V_e = 1$ . We also position the RIS at a distance of 0.3 and 0.8 times of the distance between Alice and Bob from transmitter and from receiver, respectively, to maximize its gain [1] and consider two configurations of the phase shift matrix of the RIS: (a)  $\Phi_{\text{RIS, rand}}$  with all phases to be different and random; and (b)  $\Phi_{\text{RIS, opt}}$  as obtained using the PSO-based algorithm.

Figure 3 illustrates the variation of the SKR as a function of the transmission distance between Alice and Bob under four eavesdropping scenarios: localized eavesdropping on the direct channel  $\mathbf{H}_d$ , the Alice-RIS channel  $\mathbf{H}_t$ , the RIS-Bob channel  $\mathbf{H}_r$ , and global eavesdropping through effective channel purification corresponding to the overall channel  $\mathbf{H}$ . The results are presented for  $N_T = N_R = 8, 16, 32$ , and  $64$ , with a fixed number of RIS reflecting elements  $K = 64$ . It is observed that the SKR exhibits a similar performance trend across all four eavesdropping scenarios. In these cases, the SKR decreases monotonically with increasing transmission distance due to path loss. However, a significant improvement in SKR is achieved as the MIMO configuration increases. This improvement can be attributed to the enhanced spatial degrees of freedom and array gain provided by larger MIMO configurations, which strengthen the legitimate channel and improve the achievable secure transmission range. Among the localized eavesdropping scenarios, it is observed that the case, where Eve controls the Alice-RIS channel  $\mathbf{H}_t$ , results in relatively lower SKR compared to the cases where Eve controls the direct channel  $\mathbf{H}_d$  or the RIS-Bob channel  $\mathbf{H}_r$ . This behavior arises because compromising the Alice-RIS link affects the



$$\text{SKR}_{\text{MIMO}} = \sum_{i=1}^{r_H} \text{SKR}_i = \sum_{i=1}^{r_H} \left( \frac{1}{2} \log_2 \left( 1 + \frac{\beta_i V_a}{(\beta_i V_0 + (1 - \beta_i) V_e + \sigma_b^2)} \right) - h_o(\lambda_{1_i}) - h_o(\lambda_{2_i}) + h_o(\lambda_{3_i}) + h_o(\lambda_{4_i}) \right) \quad (49)$$

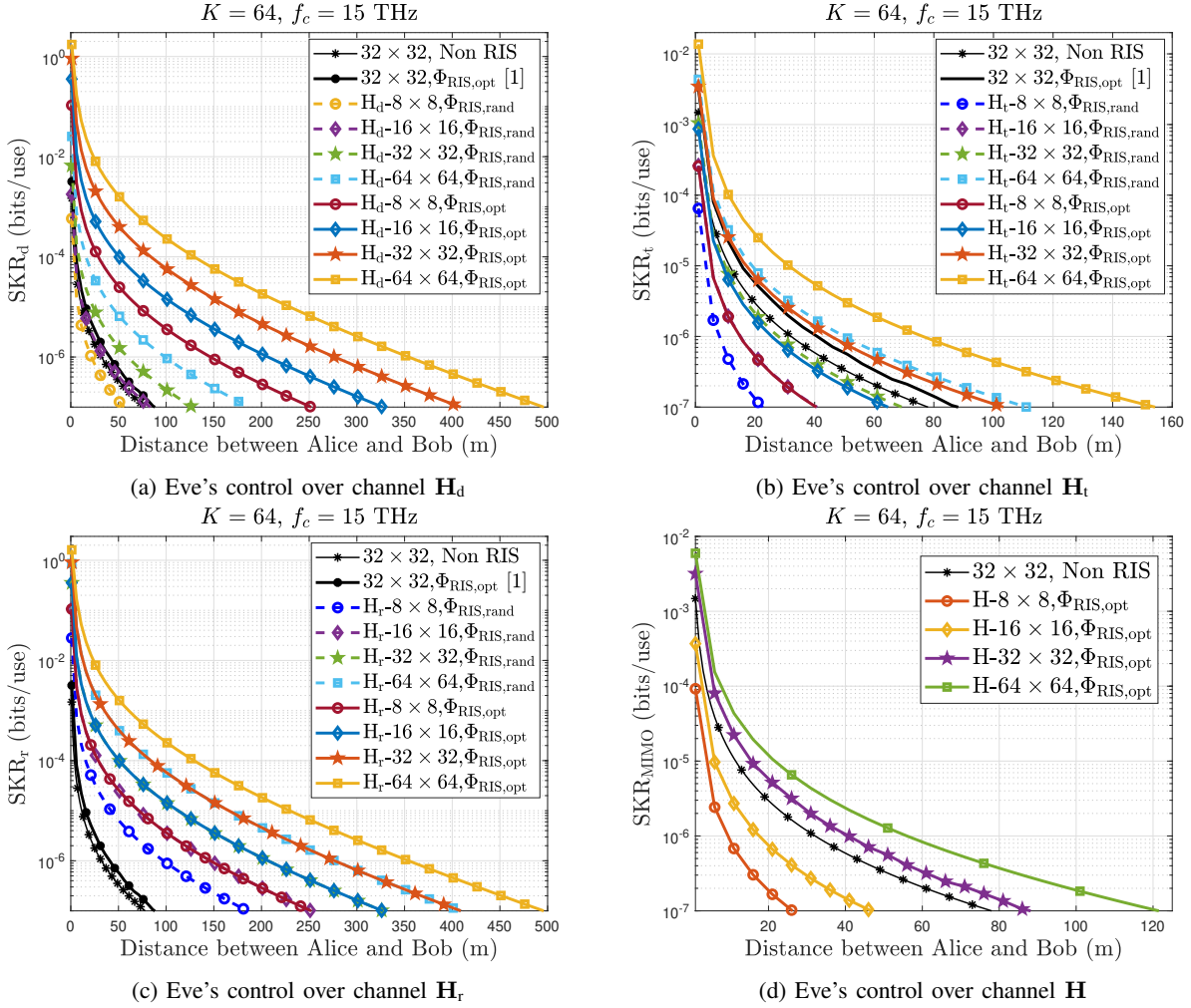


Fig. 3: SKR versus distance between Alice and Bob for  $N_R = N_T = 8, 16, 32, 64$ ,  $K = 64$ ,  $f_c = 15$  THz, and  $d_a = 0.5\lambda_c$  for Eve controls the channel (a)  $\mathbf{H}_d$ , (b)  $\mathbf{H}_t$ , (c)  $\mathbf{H}_r$ , and  $\mathbf{H}$ .

signal before RIS reflection and beamforming gain can be fully exploited, thereby degrading the overall effective channel between Alice and Bob. Furthermore, the SKR values obtained under the localized eavesdropping scenarios are considerably higher than those reported under the global eavesdropping model in [1], where Eve is assumed to have access to the purification of the overall channel. This comparison shows that restricting the eavesdropper's access to specific channel segments yields a substantial improvement in SKR for RIS-assisted THz MIMO CV-QKD systems. Additionally, it is observed that the RIS phase configuration obtained using the proposed particle swarm optimization (PSO) algorithm consistently outperforms random phase configurations across all considered MIMO configurations and eavesdropping scenarios.

Figure 4 illustrates the variation of the SKR as a function of the transmission distance between Alice and Bob under

four eavesdropping scenarios: localized eavesdropping on the direct channel  $\mathbf{H}_d$ , the Alice–RIS channel  $\mathbf{H}_t$ , the RIS–Bob channel  $\mathbf{H}_r$ , and global eavesdropping through effective channel purification corresponding to the overall channel  $\mathbf{H}$ . The plots are presented for different numbers of RIS reflecting elements  $K = 9, 25, 64, 100, 225$ ,  $8 \times 8$  MIMO configuration, and optimal RIS phase  $\Phi_{\text{RIS, opt}}$ . Similar to Fig. 3, the SKR decreases monotonically with increasing transmission distance due to the severe propagation loss at THz frequencies. It is observed that when Eve controls either the direct Alice–Bob channel  $\mathbf{H}_d$  or the RIS–Bob channel  $\mathbf{H}_r$ , the SKR curves corresponding to different values of  $K$  tends to overlap along the distances. This indicates that the benefit of RIS beamforming becomes limited when the final propagation segment toward Bob or the direct path itself is compromised by the eavesdropper. In contrast, when Eve controls the Alice–RIS channel  $\mathbf{H}_t$  or performs global channel purification through the

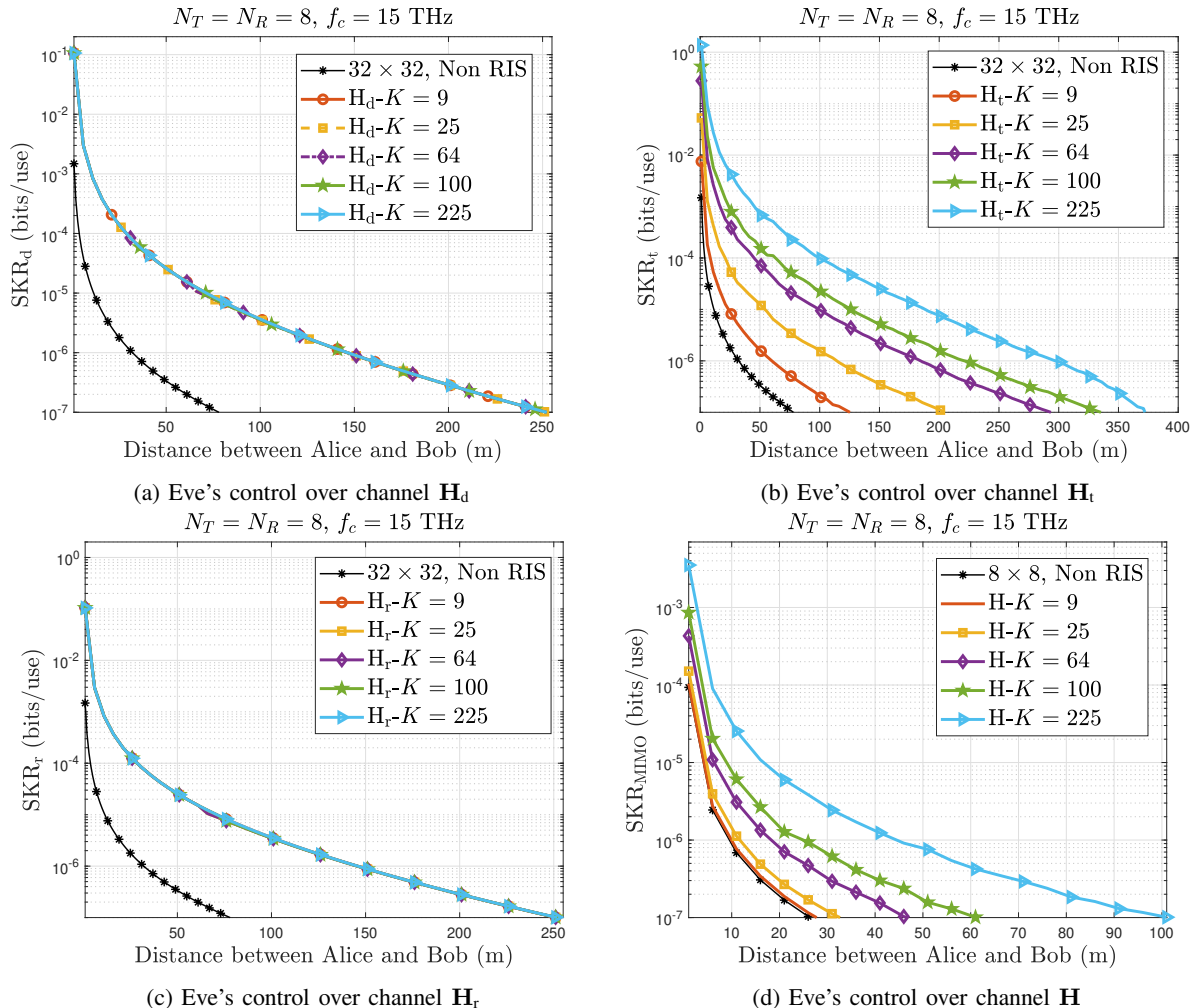


Fig. 4: SKR versus distance between Alice and Bob for  $K = 9, 25, 64, 100, 225$ ,  $N_R = N_T = 8$ ,  $f_c = 15 \text{ THz}$ , and  $d_a = 0.5\lambda_c$  for Eve controls the channel (a)  $\mathbf{H}_d$ , (b)  $\mathbf{H}_t$ , (c)  $\mathbf{H}_r$ , and (d)  $\mathbf{H}$ .

effective channel  $\mathbf{H}$ , increasing the number of RIS reflecting elements leads to a noticeable improvement in SKR. In these cases, larger RIS sizes provide stronger passive beamforming gain, resulting in higher SKR values at a given distance and extending the maximum secure communication range, particularly in the long-distance regime where RIS assistance compensates for the severe THz path loss. These observations further demonstrate that localized eavesdropping results in significantly higher achievable SKR compared to the worst-case global attack model considered in [1].

Figure 5 depicts the performance comparison for the non-RIS case and RIS-assisted transmission under optimal,  $\Phi_{\text{RIS,opt}}$  and random  $\Phi_{\text{RIS,rand}}$ , RIS phase configurations for  $\mathbf{H}_d$ ,  $\mathbf{H}_t$ ,  $\mathbf{H}_r$  channel, and overall channel  $\mathbf{H}$ . It is observed that the non-RIS system exhibits a rapid SKR degradation and supports secure key transmission only over short distances, whereas RIS-assisted transmission significantly enhances the SKR and extends the secure communication range. Among the RIS-assisted schemes, the PSO-optimized phase configuration  $\Phi_{\text{RIS,opt}}$  consistently achieves the highest SKR across the entire distance range, while random phase control  $\Phi_{\text{RIS,rand}}$  yields lower SKR but still clearly outperforms the non-

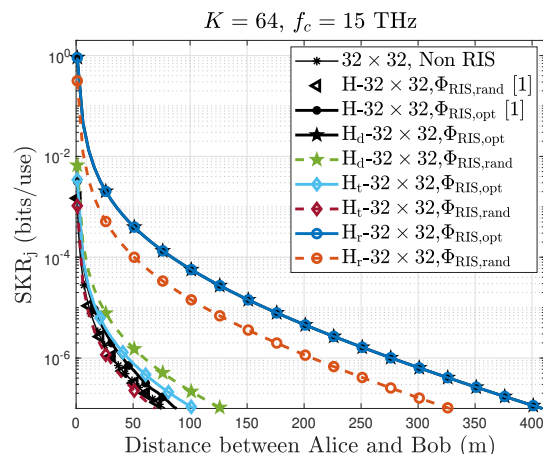


Fig. 5: SKR versus the distance between Alice and Bob with  $N_T = N_R = 32 \times 32$ ,  $K = 64$ , and  $f_c = 15 \text{ THz}$ .

RIS case, whereas Evs's control on Alice-RIS channel  $\mathbf{H}_t$  underperformed. It is further observed that the SKR trends corresponding to the channels  $\mathbf{H}_d$  and  $\mathbf{H}_r$  are identical, indicating that RIS phase optimization has a dominant influence

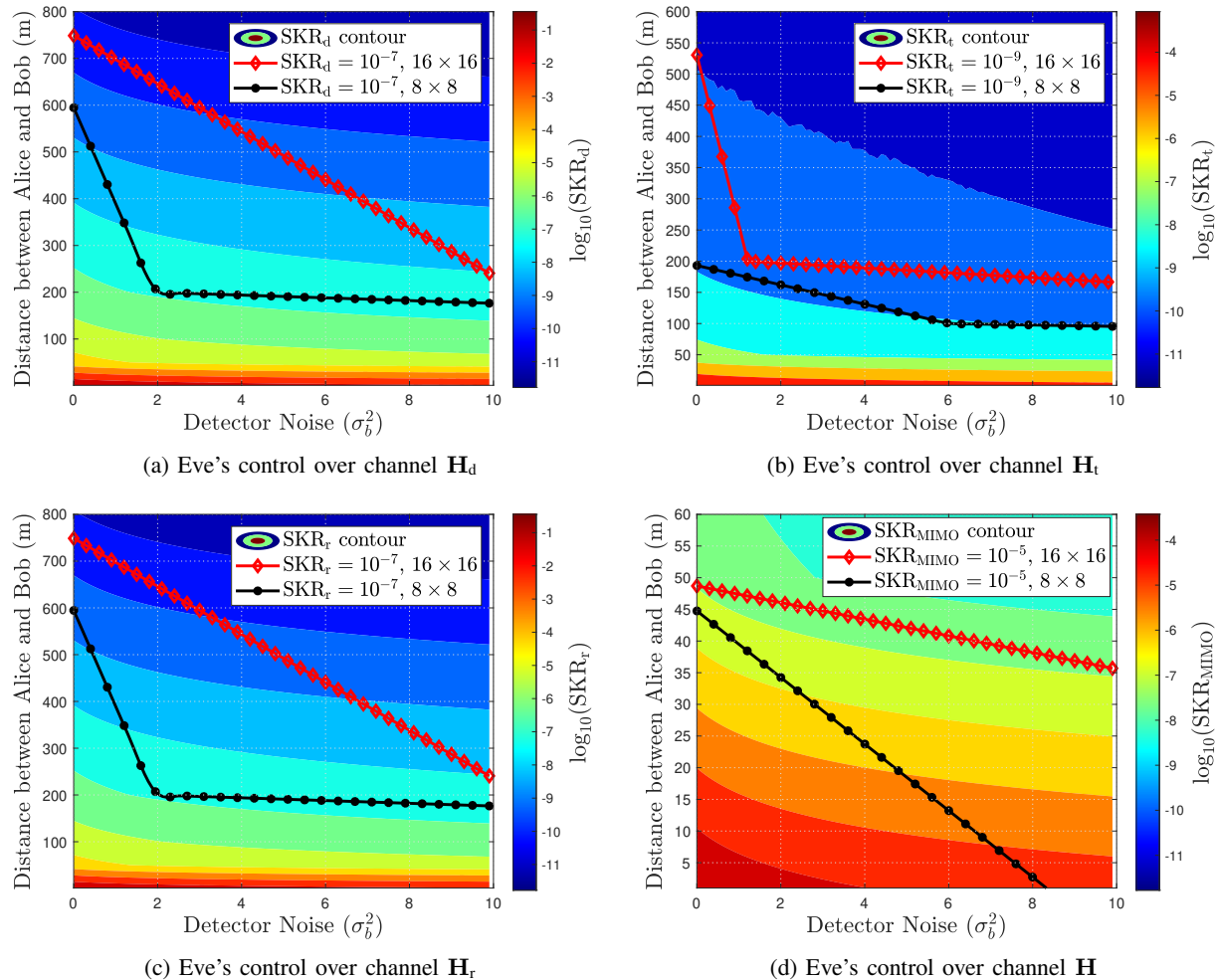


Fig. 6: Distance between Alice and Bob versus detector noise  $\sigma_b^2$  for  $N_R = N_T = 8, 16$ ,  $K = 64$ ,  $f_c = 15$  THz, and  $d_a = 0.5\lambda_c$  for Eve controls the channel (a)  $\mathbf{H}_d$ , (b)  $\mathbf{H}_t$ , (c)  $\mathbf{H}_r$ , and (d)  $\mathbf{H}$ .

on SKR (more on channel  $\mathbf{H}_d$ ) as compared to the channel  $\mathbf{H}_t$ . Moreover, RIS-assisted localized eavesdropping achieves significantly higher SKR as compared to global eavesdropping, due to effective channel purification of the overall channel  $\mathbf{H}$ , as shown in [1]. These results show that optimizing the RIS phase configuration is crucial for maximizing the SKR performance of RIS-assisted THz MIMO CV-QKD systems.

Figure 6 depicts the maximum secure transmission distance versus detector noise variance  $\sigma_b^2$  at the particular security threshold for  $N_R = N_T = 8$  and 16, with  $K = 64$  and  $f_c = 15$  THz, under all four eavesdropping scenarios. In all cases, the secure distance decreases monotonically with increasing detector noise, reflecting the degradation of Bob's received signal quality. Increasing the MIMO configuration significantly extends the secure operating region and enhances robustness against noise. It is also observed that among the localized eavesdropping scenarios shown in Fig. 4a-4c, the achievable secure distance exhibits similar trends, although the performance varies depending on the compromised channel segment. When Eve controls the Alice-RIS channel  $\mathbf{H}_t$ , the achievable secure distance becomes slightly more restricted compared to the cases where Eve controls the direct channel

$\mathbf{H}_d$  or the RIS-Bob channel  $\mathbf{H}_r$ . This occurs because compromising the first hop of the RIS-assisted link reduces the signal strength before the RIS reflection gain can be fully exploited. While in Fig. 4d the achievable secure distance is significantly reduced compared to the localized eavesdropping scenarios, and the SKR contours shift toward smaller distances as the detector noise increases. This result shows that global channel purification represents a more powerful eavesdropping strategy.

## V. CONCLUSION

In this paper, the SKR performance of an RIS-assisted THz MIMO CV-QKD system was analyzed under both localized and global eavesdropping scenarios. Closed-form expressions for the achievable SKR were derived for homodyne detection and reverse reconciliation under both localized eavesdropping and the global channel purification model. The presented numerical results demonstrated that RIS assistance contributes significantly to enhancing SKR performance and extends the secure transmission range in THz MIMO systems. Further improvements were observed with increasing MIMO dimensions and RIS sizes, particularly at long distances, in terms of the

number of metamaterial elements. The proposed PSO-based RIS phase configuration optimization method consistently outperformed random phase configurations, and performance degradation became more pronounced as noise variance increased. Moreover, substantially higher SKR values were obtained under localized eavesdropping compared to the worst-case global attack model. Overall, RIS-assisted THz MIMO CV-QKD is established as a promising framework for secure next-generation wireless networks, where RISs can be effectively leveraged to enhance quantum secrecy performance. Future research will focus on SKR performance under imperfect CSI conditions and practical RIS hardware constraints [55], including discrete phase quantization, reflection losses, and realistic unit element responses.

## REFERENCES

- [1] S. Kumar, S. P. Dash, and G. C. Alexandropoulos, "RIS-empowered CV-QKD THz MIMO communications: SKR analysis and optimization," in *Proc. IEEE Wireless Commun. Netw. Conf.*, Kuala Lumpur, Malaysia, Apr. 2026, to be presented.
- [2] M. Giordani, M. Polese, M. Mezzavilla, S. Rangan, and M. Zorzi, "Toward 6G networks: Use cases and technologies," *IEEE Commun. Mag.*, vol. 58, no. 3, pp. 55–61, Mar. 2020.
- [3] S. P. Dash, S. Joshi, S. C. Satapathy, S. K. Shandilya, and G. Panda, "A cybertwin-based 6G cooperative IoE communication network: Secrecy outage analysis," *IEEE Trans. Indus. Inform.*, vol. 18, no. 7, pp. 4922–4932, Jul. 2022.
- [4] M. Guo and M. C. Gursoy, "Joint activity detection and channel estimation in cell-free massive MIMO networks with massive connectivity," *IEEE Trans. Commun.*, vol. 70, no. 1, pp. 317–331, Jan. 2022.
- [5] J. Xu, L. You, G. C. Alexandropoulos, X. Yi, W. Wang, and X. Gao, "Near-field wideband extremely large-scale MIMO transmissions with holographic metasurface-based antenna arrays," *IEEE Trans. Wireless Commun.*, vol. 23, no. 9, pp. 12 054–12 067, Sep. 2024.
- [6] I. F. Akyildiz, C. Han, Z. Hu, S. Nie, and J. M. Jornet, "Terahertz band communication: An old problem revisited and research directions for the next decade," *IEEE Trans. Commun.*, vol. 70, no. 6, pp. 4250–4285, Jun. 2022.
- [7] M. Shehata, K. Wang, J. Webber, M. Fujita, T. Nagatsuma, and W. Withayachumnankul, "IEEE 802.15.3d-compliant waveforms for terahertz wireless communications," *J. Lightwave Technol.*, vol. 39, no. 24, pp. 7748–7760, Dec. 2021.
- [8] S. P. Chepuri, N. Shlezinger, F. Liu, G. C. Alexandropoulos, S. Buzzi, and Y. C. Eldar, "Integrated sensing and communications with reconfigurable intelligent surfaces: From signal modeling to processing," *IEEE Signal Process. Mag.*, vol. 40, no. 6, pp. 41–62, Sep. 2023.
- [9] E. Calvanese Strinati, G. C. Alexandropoulos, N. Amani, M. Crozzoli, G. Madhusudan, S. Mekki, F. Rivet, V. Sciancalepore, P. Sehier, M. Stark, and H. Wymeersch, "Toward distributed and intelligent integrated sensing and communications for 6G networks," *IEEE Wireless Commun.*, vol. 32, no. 1, pp. 60–67, Feb. 2025.
- [10] B. R. Reddy, S. P. Dash, and D. Ghose, "Optimal multi-level amplitude-shift keying for non-coherent SIMO wireless system in Rician fading environment," *IEEE Trans. Veh. Technol.*, vol. 73, no. 3, pp. 4493–4498, Mar. 2024.
- [11] S. Xue, Y. Ma, N. Yi, and R. Tafazolli, "Unsupervised deep learning for MU-SIMO joint transmitter and noncoherent receiver design," *IEEE Wireless Commun. Lett.*, vol. 8, no. 1, pp. 177–180, Feb. 2019.
- [12] K. Chen-Hu, G. C. Alexandropoulos, and A. G. Armada, "Non-coherent modulation with random phase configurations in RIS-empowered cellular MIMO systems," *ITU J. Future Evolving Technol.*, vol. 3, no. 2, pp. 1–14, Sep. 2022.
- [13] R.-Y. Wei, W.-Y. Chin, and T.-Y. Feng, "Noncoherent two-way relaying with decode and forward: Two versus three phases," *IEEE Trans. Veh. Technol.*, vol. 71, no. 3, pp. 3350–3354, Mar. 2022.
- [14] E. Basar, G. C. Alexandropoulos, Y. Liu, Q. Wu, S. Jin, C. Yuen, O. A. Dobre, and R. Schober, "Reconfigurable intelligent surfaces for 6G: Emerging hardware architectures, applications, and open challenges," *IEEE Veh. Technol. Mag.*, vol. 19, no. 3, pp. 27–47, Sep. 2024.
- [15] G. C. Alexandropoulos, A. Zappone, N. Shlezinger, M. Di Renzo, and Y. C. Eldar, *Reconfigurable Intelligent Surfaces for Wireless Communications: Modeling, Architectures, and Applications*. Singapore: Springer Nature, 2026.
- [16] A. Rabault, L. Le Magoarou, J. Sol, G. C. Alexandropoulos, N. Shlezinger, H. Vincent Poor, and P. del Hougne, "On the tacit linearity assumption in common cascaded models of RIS-parametrized wireless channels," *IEEE Trans. Wireless Commun.*, vol. 23, no. 8, pp. 10 001–10 014, Aug. 2024.
- [17] A. P. Ajayan, S. P. Dash, and B. Ramkumar, "Approximate composite channel statistics and performance analysis of IRS-aided wireless system under Nakagami- $m$  fading," *IEEE Access*, vol. 11, pp. 102 290–102 300, Sep. 2023.
- [18] S. P. Dash and A. Kaushik, "RIS-assisted 6G wireless communications: A novel statistical framework in the presence of direct channel," *IEEE Commun. Lett.*, vol. 28, no. 3, pp. 717–721, Jan. 2024.
- [19] G. C. Alexandropoulos, D.-T. Phan-Huy, K. D. Katsanos, M. Crozzoli, H. Wymeersch, P. Popovski, P. Ratajczak, Y. Bénédic, M.-H. Hamon, S. H. Gonzalez, P. Mursia, M. Rossanese, V. Sciancalepore, J.-B. Gros, S. Terranova, G. Gradoni, P. D. Lorenzo, M. Rahal, B. Denis, R. D'Errico, A. Clemente, and E. C. Strinati, "RIS-enabled smart wireless environments: Deployment scenarios, network architecture, bandwidth and area of influence," *EURASIP J. Wireless Commun. Netw.*, vol. 2023, p. 103, Oct. 2023.
- [20] Q. Zhu, M. Li, R. Liu, and Q. Liu, "Joint transceiver beamforming and reflecting design for active RIS-aided ISAC systems," *IEEE Trans. Veh. Technol.*, vol. 72, no. 7, pp. 9636–9640, Jul. 2023.
- [21] S. P. Dash, R. K. Mallik, and N. Pandey, "Performance analysis of an index modulation-based receive diversity RIS-assisted wireless communication system," *IEEE Commun. Lett.*, vol. 26, no. 4, pp. 768–772, Apr. 2022.
- [22] S. P. Dash, S. Joshi, and S. Aissa, "Envelope distribution of two correlated complex Gaussian random variables and application to the performance evaluation of RIS-assisted communications," *IEEE Commun. Lett.*, vol. 26, no. 9, pp. 2018–2022, Sep. 2022.
- [23] A. Basu, S. P. Dash, A. Kaushik, D. Ghose, M. D. Renzo, and Y. C. Eldar, "Performance analysis of RIS-aided index modulation with greedy detection over Rician fading channels," *IEEE Trans. Wireless Commun.*, vol. 23, no. 8, pp. 8465–8479, Jan. 2024.
- [24] R. Singh, A. Kaushik, W. Shin, G. C. Alexandropoulos, M. Toka, and M. Di Renzo, "Indexed multiple access with reconfigurable intelligent surfaces: The reflection tuning potential," *IEEE Commun. Mag.*, vol. 62, no. 4, pp. 120–126, Apr. 2024.
- [25] A. Basu, S. P. Dash, and D. Ghose, "RIS empowered index modulation-based receive diversity wireless system with Nakagami- $m$  fading channels," *IEEE Trans. Veh. Technol.*, pp. 1–15, Jun. 2024.
- [26] Y. Liu, C. Huang, G. Chen, R. Song, S. Song, and P. Xiao, "Deep learning empowered trajectory and passive beamforming design in UAV-RIS enabled secure cognitive non-terrestrial networks," *IEEE Wireless Commun. Lett.*, vol. 13, no. 1, pp. 188–192, Jan. 2024.
- [27] C. Weedbrook, S. Pirandola, R. García-Patrón, N. J. Cerf, T. C. Ralph, J. H. Shapiro, and S. Lloyd, "Gaussian quantum information," *Rev. Mod. Phys.*, vol. 84, no. 2, p. 621, May 2012.
- [28] A. Manzalini, "Quantum communications in future networks and services," *Quantum Rep.*, vol. 2, no. 1, pp. 221–232, Mar. 2020.
- [29] W. Diffie and M. Hellman, "New directions in cryptography," *IEEE Trans. Inf. Theory*, vol. 22, no. 6, pp. 644–654, Nov. 1976.
- [30] I. B. Djordjevic, "Hybrid QKD protocol outperforming both DV- and CV-QKD protocols," *IEEE Photon. J.*, vol. 12, no. 1, pp. 1–8, Feb. 2020.
- [31] C. Ware, R. Aymeric, C. Zidi, and M. Lourdiane, "Potential impact of CV-QKD integration on classical WDM network capacity," *IEEE Photon. Technol. Lett.*, vol. 34, no. 18, pp. 957–960, Sep. 2022.
- [32] R. Lin and J. Chen, "Modeling and minimizing spontaneous Raman scattering for QKD secured DWDM networks," *IEEE Commun. Lett.*, vol. 25, no. 12, pp. 3918–3921, Dec. 2021.
- [33] V. Scarani, H. Bechmann-Pasquinucci, N. J. Cerf, M. Dušek, N. Lütkenhaus, and M. Peev, "The security of practical quantum key distribution," *Rev. Mod. Phys.*, vol. 81, pp. 1301–1350, Sep. 2009.
- [34] E. Hugues-Salas, O. Alia, R. Wang, K. Rajkumar, G. T. Kanellos, R. Nejabati, and D. Simeonidou, "11.2 Tb/s classical channel coexistence with DV-QKD over a 7-core multicore fiber," *J. Lightwave Technol.*, vol. 38, no. 18, pp. 5064–5070, Sep. 2020.
- [35] O. Alia, R. S. Tessinari, E. Hugues-Salas, G. T. Kanellos, R. Nejabati, and D. Simeonidou, "Dynamic DV-QKD networking in trusted-node-free software-defined optical networks," *J. Lightwave Technol.*, vol. 40, no. 17, pp. 5816–5824, Sep. 2022.

- [36] I. B. Djordjevic, "Optimized-eight-state CV-QKD protocol outperforming Gaussian modulation based protocols," *IEEE Photon. J.*, vol. 11, no. 4, pp. 1–10, Jun. 2019.
- [37] J. Lodewyck, M. Bloch, R. García-Patrón, S. Fossier, E. Karpov, E. Diamanti, T. Debuisschert, N. J. Cerf, R. Tualle-Brouri, S. W. McLaughlin *et al.*, "Quantum key distribution over 25 km with an all-fiber continuous-variable system," *Phys. Rev. A*, vol. 76, no. 4, p. 042305, Oct. 2007.
- [38] Z. Yichen, B. Yiming, L. Zhengyu, Y. Song, and G. Hong, "Continuous-variable quantum key distribution system: Past, present, and future," *Appl. Phys. Rev.*, vol. 11, no. 011318, Mar. 2024.
- [39] S. Pirandola, "Limits and security of free-space quantum communications," *Phys. Rev. Res.*, vol. 3, no. 1, p. 013279, May 2021.
- [40] Z. Pan and I. B. Djordjevic, "Secret key distillation over satellite-to-satellite free-space optics channel with a limited-sized aperture eavesdropper in the same plane of the legitimate receiver," *Opt. Express*, vol. 28, no. 25, pp. 37 129–37 148, Nov. 2020.
- [41] S. Pirandola, "Satellite quantum communications: Fundamental bounds and practical security," *Phys. Rev. Res.*, vol. 3, no. 2, p. 023130, May 2021.
- [42] J. Gariano, M. Neifeld, and I. Djordjevic, "Engineering trade studies for a quantum key distribution system over a 30 km free-space maritime channel," *App. Opt.*, vol. 56, no. 3, pp. 543–557, Jan. 2017.
- [43] J. Gariano and I. B. Djordjevic, "Trade study of aperture size, adaptive optics and multiple spatial modes for a polarization entanglement QKD system over a 30 km maritime channel," *App. Opt.*, vol. 57, no. 28, pp. 8451–8459, Oct. 2018.
- [44] S. Kumar, S. P. Dash, and G. C. Alexandropoulos, "MIMO FSO systems in hybrid quantum noise environments: SKR analysis with one- and two-way CV-QKD protocols," 2026. [Online]. Available: <https://arxiv.org/abs/2509.07408>
- [45] K. P. Peppas, G. C. Alexandropoulos, E. D. Xenos, and A. Maras, "The fischer–snedecor  $\mathcal{F}$ -distribution model for turbulence-induced fading in free-space optical systems," *J. Lightwave Technol.*, vol. 38, no. 6, pp. 1286–1295, Mar. 2020.
- [46] M. Zhang, S. Pirandola, and K. Delfanazari, "Millimeter-waves to terahertz SISO and MIMO continuous variable quantum key distribution," *IEEE Trans. Quantum Eng.*, vol. 4, pp. 1–10, Apr. 2023.
- [47] C. Ottaviani, M. J. Woolley, M. Erementchouk, J. F. Federici, P. Mazumder, S. Pirandola, and C. Weedbrook, "Terahertz quantum cryptography," *IEEE J. Sel. Areas Commun.*, vol. 38, no. 3, pp. 483–495, Mar. 2020.
- [48] Z. Wang, R. Malaney, and J. Green, "Inter-satellite quantum key distribution at terahertz frequencies," in *ICC 2019 - 2019 IEEE Int. Conf. Commun.* IEEE, May 2019.
- [49] M. T. Sayat, B. Shajilal, S. P. Kish, S. M. Assad, T. Symul, P. K. Lam, N. J. Rattenbury, and J. E. Cater, "Satellite-to-ground continuous variable quantum key distribution: The Gaussian and discrete modulated protocols in low earth orbit," *IEEE Trans. Commun.*, vol. 72, no. 6, pp. 3244–3255, Jun. 2024.
- [50] N. K. Kundu, S. P. Dash, M. R. McKay, and R. K. Mallik, "MIMO terahertz quantum key distribution," *IEEE Commun. Lett.*, vol. 25, no. 10, pp. 3345–3349, Oct. 2021.
- [51] S. Kumar and S. P. Dash, "SKR analysis of one- and two-way CV-QKD MIMO FSO communication system," *IEEE Commun. Lett.*, vol. 29, no. 10, pp. 2456–2460, Oct. 2025.
- [52] S. Kumar, S. P. Dash, and G. C. Alexandropoulos, "Performance analysis of one- and two-way DV-QKD with MIMO FSO communication systems," in *Proc. IEEE International Conf. Commun.*, Glasgow, Scotland, UK, May 2026, to be presented.
- [53] A. M. Sayeed, "Quantum MIMO: A framework for entanglement distribution in spatial multipath channels," in *Quantum 2.0 Conference and Exhibition*. Optica Publishing Group, 2022, p. QTu2A.20.
- [54] S. Kumar, S. P. Dash, D. Ghose, and G. C. Alexandropoulos, "RIS-assisted MIMO CV-QKD at THz frequencies: Channel estimation and secret key rate analysis," *IEEE Trans. Commun.*, vol. 73, no. 12, pp. 15 612–15 624, Dec. 2025.
- [55] G. C. Alexandropoulos, B. K. Jung, P. Gavriilidis, S. Matos, L. H. Loeser, V. Elesina, A. Clemente, R. D'Errico, L. M. Pessoa, and T. Kürner, "Characterization of indoor reconfigurable intelligent surface-assisted channels at 304 GHz: Experimental measurements, challenges, and future directions," *IEEE Veh. Technol. Mag.*, vol. 20, no. 3, pp. 20–29, Sep. 2025.
- [56] S. W. Ellingson, "Path loss in reconfigurable intelligent surface-enabled channels," in *Proc. IEEE Int. Symp. Personal, Indoor Mobile Radio Commun. (PIMRC)*. Helsinki, Finland, Sep. 2021, pp. 829–835.
- [57] M. He, J. Xu, W. Xu, H. Shen, N. Wang, and C. Zhao, "RIS-assisted quasi-static broad coverage for wideband mmWave massive MIMO systems," *IEEE Trans. Wireless Commun.*, vol. 22, no. 4, pp. 2551–2565, Apr. 2023.
- [58] N. Hosseini-dehaj, Z. Babar, R. Malaney, S. X. Ng, and L. Hanzo, "Satellite-based continuous-variable quantum communications: State-of-the-art and a predictive outlook," *IEEE Commun. Surveys Tut.*, vol. 21, no. 1, pp. 881–919, Aug. 2019.
- [59] C. Gianfranco, *Quantum Communications*. University of Padova, Padova, Italy: Springer, 2015, ch. Fundamentals of Continuous Variables, pp. 475–484.
- [60] S. Pirandola, S. L. Braunstein, and S. Lloyd, "Characterization of collective Gaussian attacks and security of coherent-state quantum cryptography," *Phys. Review Lett.*, vol. 101, no. 20, p. 200504, Nov. 2008.
- [61] C. Weedbrook, S. Pirandola, S. Lloyd, and T. C. Ralph, "Quantum cryptography approaching the classical limit," *Phys. Rev. Lett.*, vol. 105, p. 11, Sep. 2010.